Can desert dust explain the outgoing longwave radiation anomaly over the Sahara during July 2003?

Jim M. Haywood,[1] Richard P. Allan,[2] Ian Culverwell,[1] Tony Slingo,[2] Sean Milton,[1] John Edwards,[1] and Nicolas Clerbaux[3]

Received 14 July 2004; revised 21 October 2004; accepted 2 December 2004; published 9 March 2005.

[1] Measurements of the top-of-the-atmosphere outgoing longwave radiation (OLR) for July 2003 from Meteosat-7 are used to assess the performance of the numerical weather prediction version of the Met Office Unified Model. A significant difference is found over desert regions of northern Africa where the model emits too much OLR by up to 35 Wm^{-2} in the monthly mean. By cloud-screening the data we find an error of up to 50 Wm^{-2} associated with cloud-free areas, which suggests an error in the model surface temperature, surface emissivity, or atmospheric transmission. By building up a physical model of the radiative properties of mineral dust based on in situ, and surface-based and satellite remote sensing observations we show that the most plausible explanation for the discrepancy in OLR is due to the neglect of mineral dust in the model. The calculations suggest that mineral dust can exert a longwave radiative forcing by as much as 50 Wm^{-2} in the monthly mean for 1200 UTC in cloud-free regions, which accounts for the discrepancy between the model and the Meteosat-7 observations. This suggests that inclusion of the radiative effects of mineral dust will lead to a significant improvement in the radiation balance of numerical weather prediction models with subsequent improvements in performance.

Citation: Haywood, J. M., R. P. Allan, I. Culverwell, T. Slingo, S. Milton, J. Edwards, and N. Clerbaux (2005), Can desert dust explain the outgoing longwave radiation anomaly over the Sahara during July 2003?, *J. Geophys. Res.*, *110*, D05105, doi:10.1029/2004JD005232.

1. Introduction

[2] The top of the atmosphere radiative energy balance between net incoming solar radiation and outgoing longwave radiation (OLR) is crucial in determining the large-scale atmospheric circulation and therefore the synoptic evolution important for weather and climate prediction.

[3] Mineral dust has received considerable attention over recent years. Mineral dust is the aerosol species that has the largest optical depth and exerts the largest annual mean direct radiative effect at solar wavelengths (DRE_{SW}) over ocean according to satellite observations [e.g., *Myhre et al.*, 2004]. In addition, mineral dust aerosol particles are sufficiently large to lead to a significant direct radiative effect at terrestrial wavelengths (DRE_{LW}). The interaction of the dust laden Saharan air layer with tropical cyclones is thought to suppress convection within hurricanes by imposing low relative humidities, and strong vertical wind shear [e.g., *Dunion and Velden*, 2004].

[4] The aircraft measurements performed by *Haywood et al.* [2003a] reveal a local instantaneous DRE_{SW} from a large Saharan dust plume advected off the coast of western Africa of approximately -130 Wm^{-2}. *Highwood et al.* [2003] determined the local instantaneous DRE_{LW} of the same dust plume to be approximately -6.5 Wm^{-2}. However, DRE_{SW} will be a strong function of the solar zenith angle [e.g., *Boucher et al.*, 1998] and will only be effective during daylight, while DRE_{LW} will be effective for the full 24 hours, and thus DRE_{LW} cannot be considered to be negligible. Additionally, DRE_{LW} will be a strong function of surface temperature which means that it is likely to be stronger over warm land surfaces than over the relatively cool ocean surfaces. *Ackerman and Chung* [1992] use aerosol optical depths derived from model calculations and brightness temperatures from the advanced very high resolution radiometer (AVHRR) together with estimates of outgoing longwave radiation from the Earth Radiation Budget Experiment (ERBE) to estimate a DRE_{LW} of 20–50 Wm^{-2} over the Arabian Peninsula. *Hsu et al.* [2000] adopt a similar methodology, using data from ERBE and the Total Ozone Mapping Spectrometer (TOMS) in assessing the aerosol optical depth over land and ocean regions, finding an instantaneous, clear sky mean DRE_{LW} of -36 Wm^{-2} per unit aerosol optical depth for July 1985 over the W. Sahara when the surface temperature is close to a maximum. *Zhang and Christopher* [2003] present data from September 2000 and show areas of northern Africa where DRE_{LW} reaches approximately +30 Wm^{-2}. They also show results from a sensitivity experiment whereby

[1]Met Office, Exeter, UK.
[2]Environmental Systems Science Centre, University of Reading, Reading, UK.
[3]Royal Meteorological Institute of Belgium, Brussels, Belgium.

0148-0227/05/2004JD005232$09.00

the local DRE_{LW} approximately doubles when the surface temperature is increased from 300 K to 316 K. Thus DRE_{LW} may be significant over land areas where the surface temperature is high.

[5] In this study, Meteosat-7 data are used to assess the OLR of the NWP model and the effects of mineral dust upon the outgoing longwave radiation are estimated. Section 2 describes the Meteosat-7 observations and the NWP model. Section 3 compares the OLR from the model with the observations, and shows that differences in OLR from the model and Meteosat-7 of up to 50 Wm^{-2} at 1200 UTC come from clear-sky regions. In section 4, we describe the radiation code and vertical profiles of temperature and humidity used in the NWP model and show that they are realistic. In section 5 we assess the surface skin temperature and model surface emissivity that would be needed to balance the clear-sky OLR discrepancy and show that these alone are unlikely to explain the differences. In sections 6 dust optical parameters are derived from a combination of in situ measurements from the Saharan Dust Experiment [e.g., *Tanré et al.*, 2003] and remote sensing measurements from Aerosol Robotic Network (AERONET) [*Holben et al.*, 1998]. These are combined with satellite measurements of aerosol optical depth, τ_{aer}, determined in section 7 to calculate the radiative effects of the mineral dust in section 8. A discussion and conclusion are presented in section 9.

2. Description of Satellite and Model OLR Data

[6] Before comparing the measured and modeled OLR, it is informative to provide a brief description of the satellite data, the NWP model, and the radiation code used in the study.

2.1. Meteosat-7 Data

[7] The Meteosat-7 geostationary satellite has operated at 0° longitude 0° latitude since June 1998. Images of the Earth's disk are acquired every 30 minutes in three spectral bands: the visible (VIS, 0.45–1.0 μm), the water vapor (WV, 5.7–7.1 μm), and the infrared (IR, 10.5–12.5 μm). Thanks to an onboard black body source, the WV and IR radiance observations are calibrated to within 1% (or 2 K in brightness temperature).

[8] The estimation of the OLR from Meteosat is done in 2 steps. First the broadband longwave radiance (L) is estimated from the radiance observations in the WV and IR channels. This is often referred to as a narrowband-to-broadband (NB-to-BB) conversion and performed by a second order regression:

$$L = c0 + c1\ WV + c2\ IR + c3WV^2 + c4\ WV\ IR + c5\ IR^2, \quad (1)$$

where c0, c1, c2, c3, c4, and c5 are regression coefficients.

[9] In a second step, this radiance is converted to irradiance (the OLR) using an angular distribution model, R(VZA), of the radiance field at the top of the atmosphere:

$$OLR = \pi L/R(VZA), \quad (2)$$

where VZA is the viewing zenith angle of observation. Detailed description of the NB-to-BB conversion (equation (1)) and angular modeling (equation (2)) are given by *Bertrand et al.* [2003] and by *Clerbaux et al.* [2003].

[10] An OLR error magnitude of 4.5% is reported by *Bertrand et al.* [2003], which is attributed as follows: 1% for the Meteosat calibration, 1.5% for the NB-to-BB conversion, and 2% for the angular modeling. This last number is a typical value but is strongly dependent on the VZA. For the studied area we take advantage of a relatively good VZA of about 30°, and the angular modeling error can be refined to 1.5%. The absolute uncertainty for a clear desert OLR of 300 Wm^{-2} is then ±12 Wm^{-2}, when estimated from Meteosat-7 which can be regarded as a likely maximum uncertainty as the errors are unlikely to be correlated.

2.2. Numerical Weather Prediction Version of the Unified Model

[11] The numerical weather prediction (NWP) Unified Model used here is described in detail by R. P. Allan et al. (Exploitation of geostationary Earth radiation budget data using simulations from a numerical weather prediction model: Methodology and data validation, submitted to *Journal of Geophysical Research*, 2004, hereinafter referred to as Allan et al., submitted manuscript, 2004); however, a brief description is given here. The basis for the current formulation of the operational global NWP Unified Model became operational in August 2002. The horizontal resolution is 0.83° longitude by 0.56° latitude (90 km in the tropics) with 38 levels in the vertical. The nonhydrostatic dynamics is a two-time level semi-implicit, semi-Lagrangian formulation and is designed to conserve mass, mass weighted potential temperature, moisture and angular momentum. The data assimilation is the three-dimensional variational assimilation scheme of *Lorenc et al.* [2000]. Recent improvements have replaced the original initialization procedure, and the incremental analysis update with a digital filtering technique.

[12] For details on the layer-cloud and convective-cloud parameterizations, the land-surface exchange scheme, and orographic drag parameterizations, see Allan et al. (submitted manuscript, 2004). The formulation of the global NWP model outlined above also forms the basis of the next generation coupled climate version (HadGEM1). The radiative transfer scheme in the NWP model is described in section 4, but it is important to note that the effects of aerosols in the longwave region of the spectrum are not accounted for.

3. Comparison of Observed and Modeled OLR Budget

[13] In section 3, we examine first the OLR from both Meteosat-7 and the NWP models for both total sky conditions and then apply cloud-screening to look at the OLR for clear sky conditions, OLRc.

3.1. Comparison of Monthly Mean for July 2003

[14] The monthly mean OLR which is the mean of the 0000, 6000, 12000, and 1800 UTC diagnostics for July 2003 is shown in Figures 1a and 1b for the Meteosat-7 observations and the NWP model respectively and are henceforth referred to as OLR_{Met7} and OLR_{model}. Figures 1a and 1b show the same general features over Africa. Both

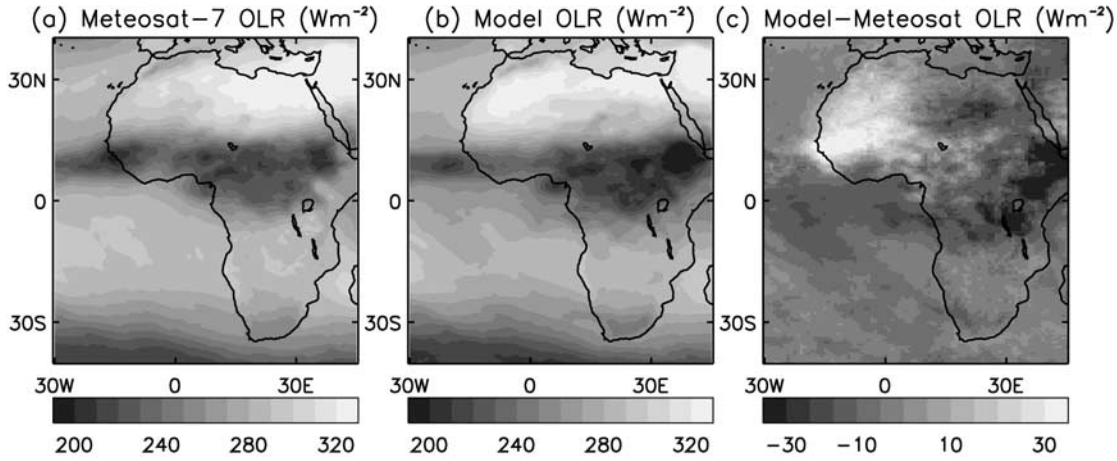

Figure 1. The July 2003 monthly mean for (a) OLR_{Met7}, (b) OLR_{model}, and (c) $OLR_{model} - OLR_{Met7}$. The monthly mean consists of the average of the monthly mean of the OLR diagnosed at 0000 UTC, 6000 UTC, 1200 UTC, and 1800 UTC. Units are Wm^{-2}. See color version of this figure in the HTML.

OLR_{Met7} and OLR_{model} are greater than 320 Wm^{-2} over hot, dry desert regions in the north and less than 200 Wm^{-2} over cold deep convective clouds of the intertropical convergence zone (ITCZ) in central equatorial Africa. Figure 1c shows the dOLR which is defined here as $OLR_{model} - OLR_{Met7}$. The two most notable features over the African continent are (1) significant negative bias associated with deep convective clouds of the ITCZ where $OLR_{model} < OLR_{Met7}$ and $|dOLR|$ exceeds 30 Wm^{-2} and (2) significant positive bias over desert regions of northwest Africa where $OLR_{model} > OLR_{Met7}$ and $|dOLR|$ exceeds 30 Wm^{-2}.

[15] The dOLR associated with the ITCZ may be explained by systematic errors in the modeling of deep convective cloud and cirrus anvils. The complex issues of moisture transport, cloud microphysical parameterizations, cloud inhomogeneities, cloud overlap assumptions and the radiance to irradiance conversion performed by the Meteosat-7 inversion procedures may all be important in explaining these discrepancies between the model and the observations. However, these issues associated with clouds are beyond the scope of the present study. Here, we concentrate on the significant positive bias over desert regions of northwest Africa. The fact that the bias in dOLR in this region is of similar magnitude and spatial extent to that associated with clouds of the ITCZ suggests that the model errors here are as significant in determining the OLR as those associated with modeling complex clouds. Furthermore, while the complex issues surrounding the accurate representation of cloud in models such as those listed above are well known but difficult to solve, the error over northwest Africa suggests either an error in the model parameterizations or a missing physical mechanism.

3.2. Application of Cloud Screening

[16] To determine whether the bias in dOLR over northwest Africa is associated with cloudy or clear sky regions a cloud-screening procedure is applied whereby a pixel is considered cloud-free if the collocated data from Meteosat-7 and from the NWP model are both classified as completely cloud-free. This avoids the introduction of biases relating to inconsistent clear-sky sampling between model and satellite data [e.g., *Allan and Ringer*, 2003]. The Meteosat-7 cloud product is provided by the Royal Meteorological Institute of Belgium and is based on the Meteosat-7 radiance to flux conversion [*Ipe et al.*, 2004]. The cloud mask is based on Meteosat-7 visible channels and is therefore independent of the OLR measurements. It should be noted that errors in the cloud flag may result from misclassification of high aerosol amount as cloud, which will cause an overestimation in OLRc, and misclassification of thin cirrus as clear, which will result in an underestimation in OLRc. Over the vast majority of the Atlantic no data are available as the Meteosat-7 data are classed as partly cloudy, which is likely caused by the algorithm identifying pixels affected by mineral dust as cloud-influenced (Figure 2).

[17] The clear-sky $OLRc_{Met7}$ and $OLRc_{model}$ for 1200 UTC are shown in Figures 2a and 2b, respectively. It is important to realize that both $OLRc_{Met7}$ and $OLRc_{model}$ are effectively "snapshots" and are therefore directly comparable: at 0° longitude the local time is 1200, but at 15°E the local time is 1300 and at 30°E the local time is 1400. The differences between $OLRc_{Met7}$ and $OLRc_{model}$ are more pronounced than in Figure 1, with $OLRc_{model}$ again showing considerably higher values across North Africa than $OLRc_{Met7}$. dOLRc, which is defined as $OLRc_{model} - OLRc_{Met7}$, shows a maximum of greater than 20–50 Wm^{-2} over Mali, Mauritania, and Southern Algeria. The fact that dOLRc is so large indicates a deficiency in the clear-sky radiative transfer processes in the NWP model. The deficiency is unlikely to be associated with errors from the satellite retrieval because it is an observation with known quantifiable uncertainties. Therefore the three most likely explanations for such a deficiency in $OLRc_{model}$ are misrepresentation of surface skin temperature, surface emissivity, atmospheric transmission, or a combination of the three. In the sections that follow, we describe the radiative transfer calculations and then investigate the potential error in skin temperature and emissivity that would lead to dOLRc and compare the results against available observations. We then investigate

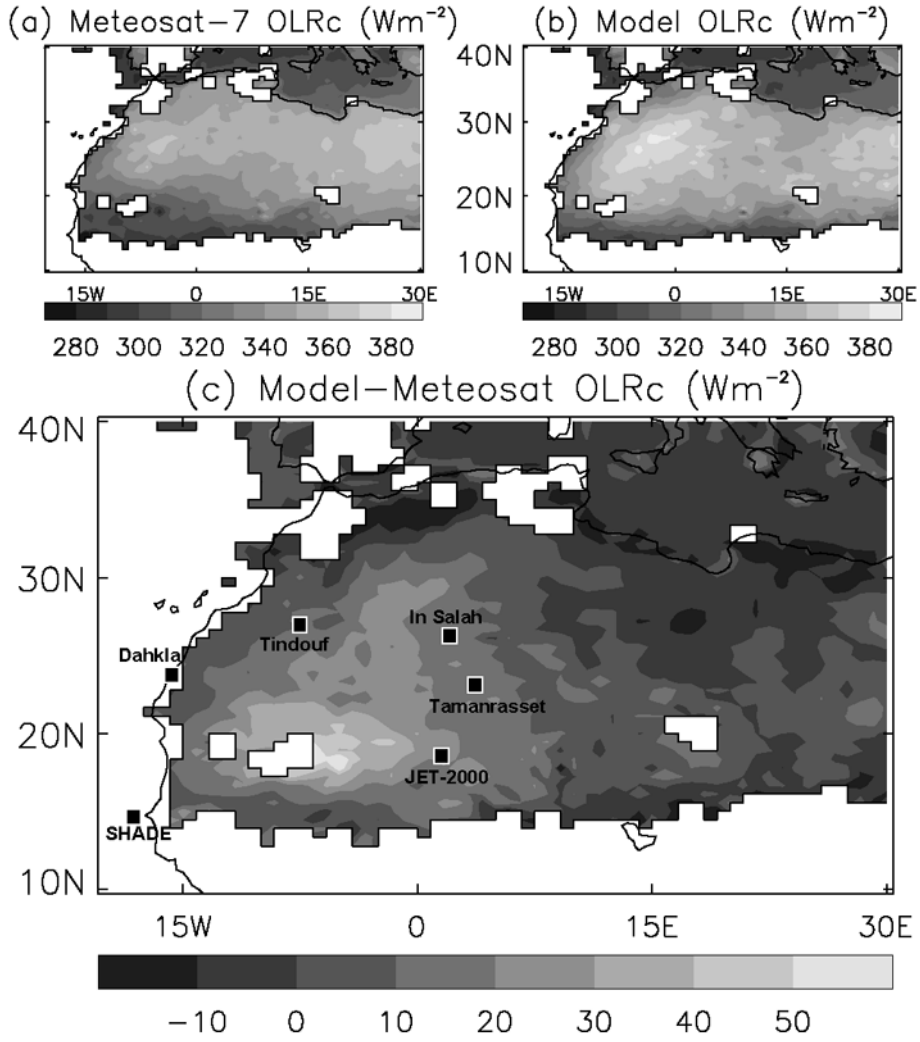

Figure 2. The July 2003 monthly mean of the 1200 UTC clear sky for (a) $OLRc_{Met7}$, (b) $OLRc_{model}$, and (c) $OLRc_{model} - OLRc_{Met7}$. Units are Wm^{-2}. Areas shown in white indicate missing/cloudy data. The approximate positions of the radiosonde stations, measurement campaigns, and AERONET sites referred to in the text are also shown. See color version of this figure in the HTML.

the radiative processes associated with atmospheric mineral dust.

4. Description of the Radiative Transfer Calculations

[18] Here we describe the physical basis of the radiative transfer code and the temperature and humidity profiles that are used as input to the code to derive the OLR.

4.1. Physical Basis of the Radiative Transfer Code

[19] The radiative transfer code used in this study is that of *Edwards and Slingo* [1996], which is based on the two-stream equations in both the longwave and shortwave spectral regions which allows for consistency in physical processes which are important in both spectral regions. Atmospheric absorption by water vapor, carbon dioxide, ozone, oxygen, nitrous oxide, methane, and CFC-11 and CFC-12 are accounted for. The scheme includes a treatment of Rayleigh scattering, nonspherical ice particles, and multiple scattering between cloud layers. The model is capable of including the scattering and absorption properties of aerosols via the specific extinction coefficient, k_e, the single scattering albedo, ω_o, and the asymmetry factor, g.

[20] The spectral resolution of the radiation code is variable; in the NWP model, there are six bands in the shortwave spectrum and nine bands in the longwave spectrum. In addition, we use a 300 band stand alone version in calculations of the effects of surface skin temperature, surface emissivity and aerosol upon the longwave irradiances, and a 220 band stand alone version in calculations of the solar irradiances. These higher spectral resolution versions of the radiation code have previously been used for calculations of the shortwave and longwave radiative effects of mineral dust aerosol by *Haywood et al.* [2001, 2003a] and *Highwood et al.* [2003]. It should be reiterated here that

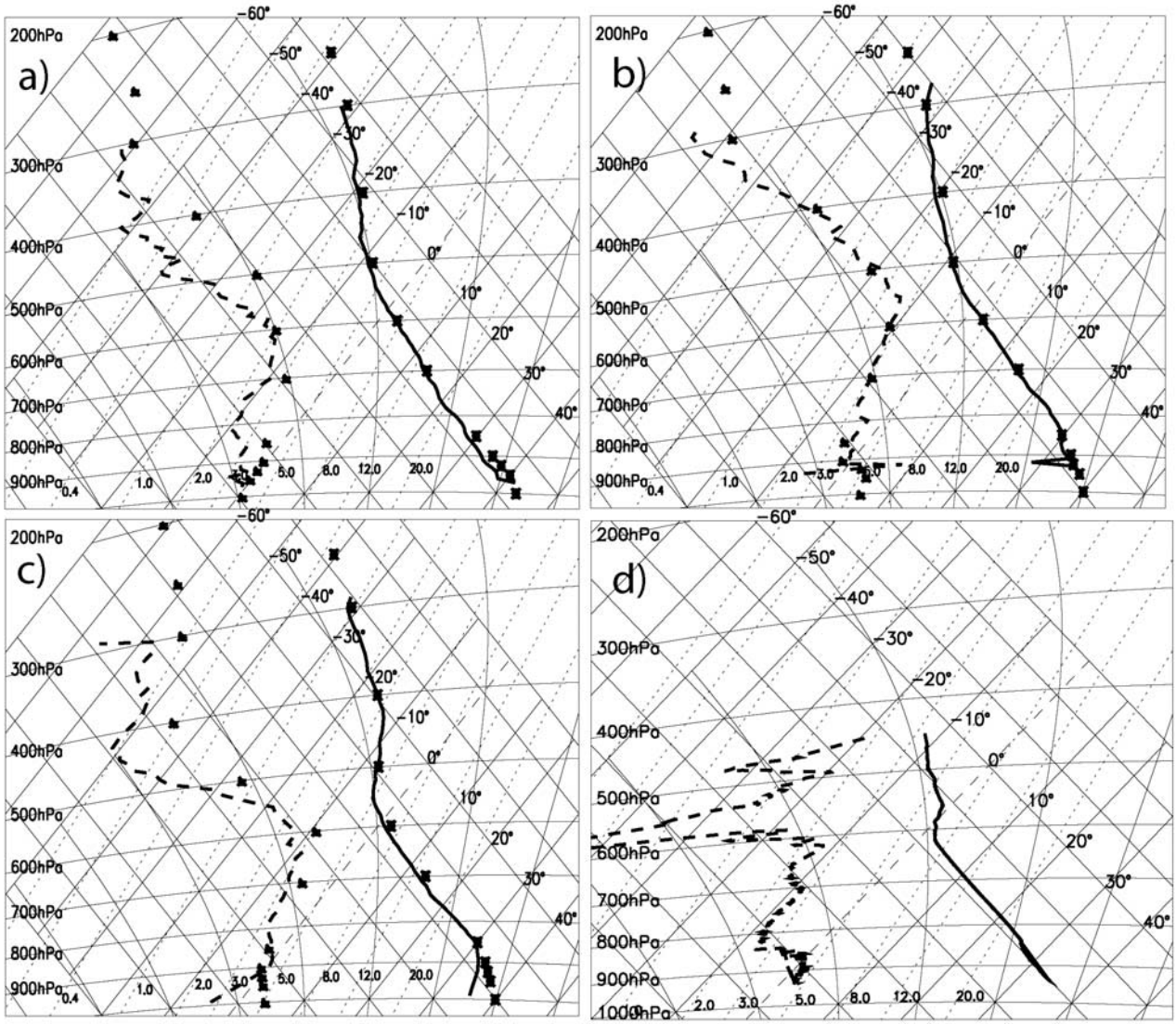

Figure 3. Tephigrams showing the vertical profiles of temperature and humidity for (a) In Salah, (b) Tindouf, (c) Tamanrasset, and (d) JET-2000. The NWP model data are shown by the symbols in Figures 3a–3c.

the scattering and absorption properties of mineral dust aerosols are not accounted for in the NWP model, but they are included in the stand alone version of the radiation code that is used to diagnose the radiative effects of aerosols in section 7.

4.2. Vertical Profiles of Temperature and Humidity

[21] The OLR is a strong function of the atmospheric temperature and humidity, and therefore it is necessary to use appropriate atmospheric profiles in radiative transfer calculations. However, observational data are extremely sparse over the Sahara Desert. In this study, we use radiosonde ascents from three nearby bases in southern Algeria located at In Salah, Tindouf, and Tamanrasset (see Figure 2c). The radiosonde ascents shown in Figures 3a–3c consist of monthly mean data from the mid-day radiosonde launches. The atmospheric profiles show characteristics typical of that shown by *Thorncroft et al.* [2003] during the JET-2000 measurement campaign shown in Figure 3d (location also marked on Figure 2c). Although there are differences between the profiles, particularly close to the surface, the following general features can be seen:

[22] 1. From the surface to ~550 hPa, the profile of atmospheric temperature is close to the dry adiabatic lapse rate.

[23] 2. Typically, the temperature of the air close to the surface is ~315 K, and because the atmospheric profile is close to dry adiabatic, the equivalent potential temperature is approximately constant up to ~550 hPa.

[24] 3. From the surface to ~550 hPa the specific humidity is typically 2–4 gcm^{-3}.

[25] We use the atmospheric profile from observations at In-Salah in the radiative transfer calculations that follow. Use of the profiles from Tindouf and Tamanrasset changes the OLRc by less than 2 Wm^{-2}. Also plotted on Figure 3 are the NWP monthly mean model analyses of temperatures and humidities for 1200 UTC. Because the NWP model

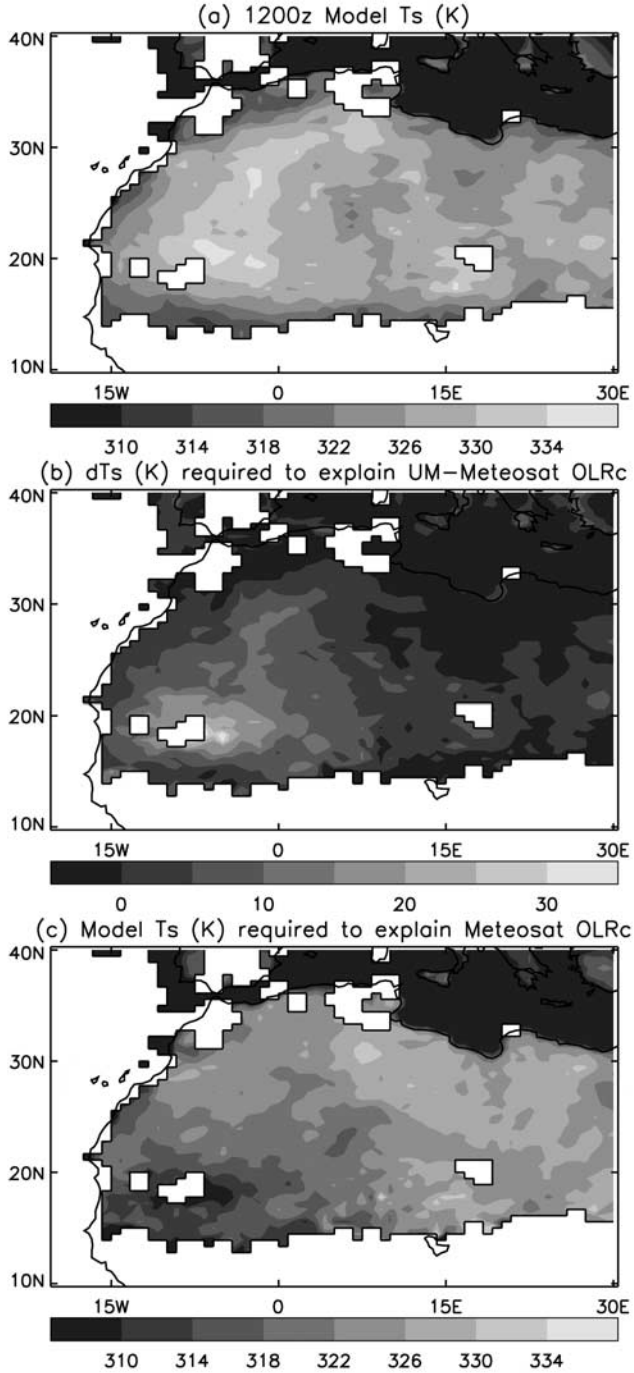

Figure 4. (a) Surface skin temperature, T_s, from the NWP model. (b) The reduction in the model temperature required to explain the difference between $OLRc_{model}$ and $OLRc_{Met7}$. (c) The model T_s required so that $OLRc_{model}$ fits $OLRc_{Met7}$. Units K. See color version of this figure in the HTML.

uses data assimilation including data from radiosondes (section 2.2), the model profiles of temperature and humidity are in very close agreement with the radiosonde assents (Figures 3a–3c). Calculations using the NWP model profiles of temperature and humidity for In Salah lead to differences in OLRc of less than 3 Wm^{-2} when compared to those using the observations. Thus the model profiles of temperature and humidity cannot be responsible for the dOLRc shown in Figure 2c.

5. Investigation of Surface Skin Temperature and Emissivity

5.1. Surface Skin Temperature, T_s

[26] The surface skin temperature for 1200 UTC from the NWP model $T_{s,model}$, is shown in Figure 4a. The region of maximum $T_{s,model}$ approximately corresponds to the region where OLRc is largest (Figure 2b) and is somewhat displaced to the north from the region that shows the maximum dOLRc (Figure 2c). The maximum $T_{s,model}$ exceeds 330 K. We use the 300 band version of the *Edwards and Slingo* [1996] radiation code to investigate the perturbation to the surface temperature, dT_s, needed to reconcile $OLRc_{Met7}$ and $OLRc_{model}$ i.e., to reduce dOLRc to zero. Figure 4b shows dT_s and Figure 4c shows $T_{s,model} + dT_s$. Figure 4b shows that $T_{s,model}$ needs to be reduced by up to -30 K in order for $OLRc_{Met7}$ and $OLRc_{model}$ to agree, resulting in a $T_s \sim 310$ K in the region where the maximum dOLRc exists.

[27] To determine whether potential errors in T_s are the reason for the discrepancy in OLRc it is necessary to assess whether $T_{s,model}$ (Figure 4a) or $T_{s,model} + dT_s$ (Figure 4c) provides the best representation of the real T_s. Physical measurements of T_s over desert regions are extremely sparse and therefore remote sensing measurements from satellite sensors are frequently used. The International Satellite Cloud Climatology Project (ISCCP) data set indicates a diurnal mean July surface skin temperature determined from satellite measurements from the period 1982–2001 [*Prigent et al.*, 2003] (see http://isccp.giss.nasa.gov) under clear-sky conditions in excess of 314 K over the Sahara desert. The monthly mean T_s from the model for the grid-box including In Salah is shown in Figure 5 by the data points and standard deviations at three hourly intervals. T_s from Tamanrasset, Tindouf, and other model grid points shows similar features and are not shown here. The diurnal mean T_s is approximately 312–313 K, which is in agreement with the ISCCP climatological data. In addition, the model shows a diurnal cycle that is in agreement with observational data

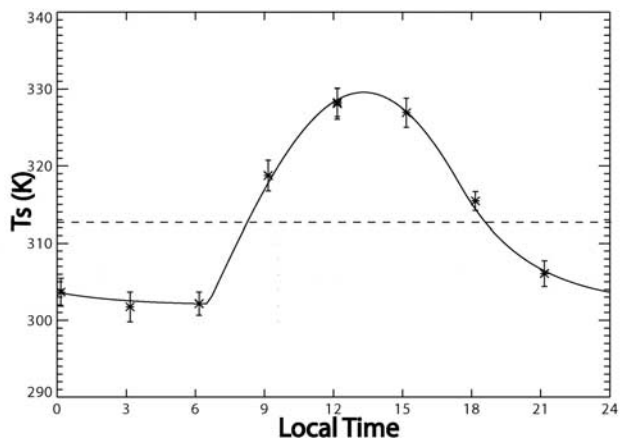

Figure 5. The diurnal variation of T_s (K) shown every 3 hours. The solid curve shows the fit from the parameterization of *Göttsche and Olesen* [2001] and the values for the fitting parameters are indicated.

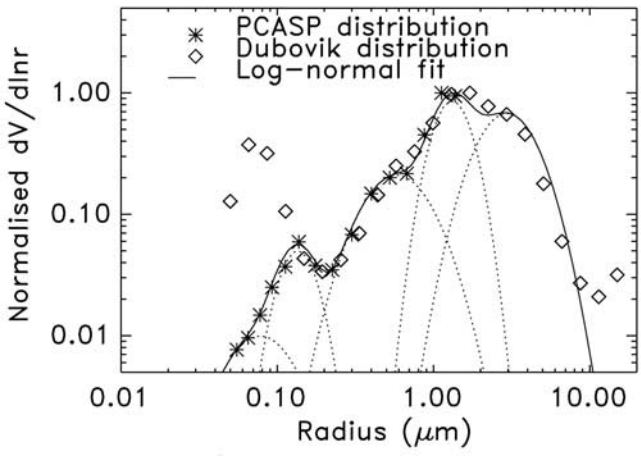

Figure 6. The aerosol size distribution used to calculate the Saharan dust optical properties. The stars represent measurements from the PCASP-100X, and the diamonds represent the monthly mean aerosol size distribution retrieved from the AERONET site at Dahkla. The five modes that are used to fit the aerosol size distribution are also shown.

from Meteosat T_s data analyzed by *Göttsche and Olesen* [2001] who fitted observational data from the Algerian desert with a cosine and exponential decay term. The fit from this parameterization and the coefficients used in fitting the parameterization are also shown on Figure 5, which shows agreement with the model data. *Prigent et al.* [2003] also present data from desert regions and document that T_s is larger than the near-surface air temperature by approximately 10–14 K close to local noon and that the difference between T_s and near-surface air temperature is almost linearly dependent on the cosine of the solar zenith angle. If we consider that the maximum T_s at In Salah and Tindouf from the model are around 328 K (Figures 4a and 5), then the near surface air temperature would be expected to be around 316 K or around 43°C. The monthly mean near surface air temperature shown in the tephigrams in Figure 3 is around 40°C which is in reasonable agreement with the observations made by *Prigent et al.* [2003]. These facts suggest that the model T_s is reasonably realistic.

5.2. Surface Emissivity, ε

[28] To investigate the effect of nonunity surface emissivity, ε, on the OLRc, the radiative transfer calculations are repeated using a broadband ε of 0.95 and 0.90 instead of 1.0 as used in the NWP model. ISCCP report ε of barren desert regions of around 0.95 for the 5–200 μm spectral region and around 0.98 for the 10–11 μm spectral region. *Sutherland* [1986] suggests similar values for ε and thus the radiative transfer calculations with ε = 0.90 can be considered an extreme lower bound. The results indicate a reduction in OLRc of approximately 7 Wm^{-2} when ε is reduced from 1.0 to 0.95, and 14 Wm^{-2} when ε is reduced from 1.0 to 0.90 for a surface temperature of 330 K. Additional calculations are made using the wavelength dependent ε from *Snyder et al.* [1998] for arid bare soil; OLRc is within 1.3 Wm^{-2} of that for a broadband ε of 0.95 for a T_s of 330 K. Thus it appears unlikely that differences in ε can explain the magnitude of dOLRc shown in Figure 2c which exceeds 50 Wm^{-2} in some regions.

6. Physical Properties, Radiative Properties, and Geographic Distribution of Mineral Dust

[29] Having determined that model errors in T_s and ε are unlikely to explain dOLRc we now investigate the final possibility; that the atmospheric transmission in the NWP model is in error. As we have seen that the model atmospheric temperature and humidity are well represented in the model as evidenced by the tephigrams shown in Figure 3, we concentrate on the radiative effects of aerosols and their effect on OLRc.

6.1. Aerosol Size Distributions

[30] As done by *Highwood et al.* [2003], two independent types of measurements of size distributions are combined with aerosol refractive indices across the solar and terrestrial spectra to determine the optical properties. The first data set is the in situ observations made on the Met Office C130 aircraft with a passive cavity aerosol spectrometer probe 100-X (PCASP) during a large dust event off the coast of Senegal during the Saharan Dust Experiment (SHADE [*Tanré et al.*, 2003]). The approximate geographical position of the measurements made during SHADE is marked on Figure 2c. Briefly, the PCASP sizes aerosols in the radius range 0.05–1.5 μm by measuring the intensity of laser radiation of wavelength 0.63 μm at scattering angles of between 35° and 120°. *Haywood et al.* [2003a, 2003b] provide details of the calibration, and potential sizing errors of the PCASP. In this study, the main limitation of using data from the PCASP is the maximum detection radius of 1.5 μm which enables determination of the aerosol radiative properties of at solar wavelengths but is too small for accurate determination of radiative properties at terrestrial wavelengths [e.g., *Haywood et al.*, 2003a; *Highwood et al.*, 2003]. This necessitates the use of supplemental aerosol size distribution data from the AERONET station at Dahkla in Mauritania (geographically the closest AERONET station to the maximum in dOLRc as shown on Figure 2). The monthly mean aerosol size distribution for July 2003 is derived using the retrieval algorithm of *Dubovik and King* [2000]. Briefly, this inversion procedure minimizes the RMS error between measured and modeled sky radiances as a function of scattering angle at a range of wavelengths. The main disadvantage of this retrieval algorithm for mineral dust particles is that nonspherical scattering effects lead to an anomalous peak in the aerosol size distribution at sizes of <0.1 μm. However, this effect is well understood and can be corrected for [*Dubovik et al.*, 2002] using a composite of prolate and oblate spheroids in place of spheres [*Mishchenko et al.*, 2003].

[31] We show the volume size distribution of the aerosol size distribution from the PCASP and the AERONET retrievals in Figure 6. Other than the anomalous peak in the AERONET size distribution at particle radii <0.1 μm, the size distribution from the SHADE campaign and the AERONET retrieval are in remarkable agreement when one considers the different geographical locations, the different time of year of the sampling, and the different methods for retrieving the aerosol size distribution. The composite

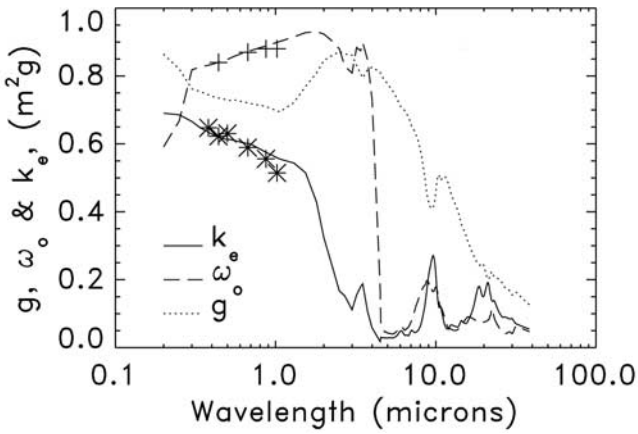

Figure 7. The aerosol optical parameters calculated using the size distribution shown in Figure 3, and the refractive indices described in the text. Specific extinction coefficient, k_e, in units of m^2 g^{-1}. Crosses show the wavelength dependence of the monthly mean aerosol optical depth calculated from the AERONET site. Single scattering albedo is ω_o. Stars show the monthly mean ω_o determined from the AERONET site; the asymmetry factor is g. The refractive indices of *Fouquart et al.* [1987] are used in these calculations.

PCASP/AERONET size distribution may be fitted with five lognormal modes as shown in Figure 6; the standard deviation and geometric mean radius of each of these modes are identical to those from *Haywood et al.* [2003a]. A further mode fitting particles greater than 10 μm radius could be included but tests show that this mode has negligible effect on the optical parameters and hence negligible effect on the radiative effects across the solar and terrestrial regions of the spectrum.

6.2. Aerosol Optical Properties

[32] The composite size distribution shown by the solid line in Figure 6 is combined with suitable refractive indices and Mie scattering theory to determine the aerosol optical parameters. As done by *Highwood et al.* [2003], we use the refractive indices of *World Climate Program* (*WCP*) [1986] for wavelengths less than 4.5 μm. However, the refractive indices of *WCP* [1986] do not adequately represent the optical characteristics of Saharan dust at terrestrial wavelengths as evidenced by interferometer measurements [*Highwood et al.*, 2003]. The refractive indices of *Fouquart et al.* [1987] and *Volz* [1973] both show a stronger absorption peak at around 10 μm due to the presence of illite and are more representative of the spectral dependence of the absorption of Saharan dust across the terrestrial spectrum [*Highwood et al.*, 2003]. Therefore, as done by *Highwood et al.* [2003], we replace the refractive indices of *WCP* [1986] at wavelengths greater than 2.5 μm with those of *Fouquart et al.* [1987] in our base case calculations. In addition, we also perform calculations using the refractive indices of *Volz* [1973] in place of those of *Fouquart et al.* [1987] to assess the effect that refractive indices have on the optical properties and associated radiative effects.

[33] Figure 7 shows the specific extinction coefficient, k_e, the single scattering albedo, ω_o, and the asymmetry factor, g, derived using the size distribution shown in Figure 7 and the combined refractive indices of *WCP* [1986] and *Fouquart et al.* [1987]. The crosses marked on Figure 7 show the variation of the aerosol optical depth at wavelength, λ, $\tau_{aer\lambda}$ from the Dahkla AERONET site. These data have been normalized so that $\tau_{aer0.55} = k_{e0.55}$ in order to demonstrate that the wavelength dependence of k_e is well represented despite the fact that monthly mean aerosol size distribution and refractive indices are used in the Mie scattering calculations while the AERONET values are determined from the mean of the daily τ_{aer}. Additionally, Figure 7 shows that ω_o calculated from the mean of the daily AERONET size distributions is in good agreement with those calculated using the monthly mean size distribution and the assumed refractive indices. This consistency suggests that the use of a single monthly mean size distribution and set of refractive index is justified.

6.3. Geographic Distribution of Mineral Dust Aerosol

[34] Many different satellite instruments have been developed that determine $\tau_{aer\lambda}$ and aerosol properties such as Angstrom coefficients and radiative effects [e.g., *Myhre et al.*, 2004]. The majority of these satellite retrievals are capable of determining aerosol radiative effects over ocean, but retrieval algorithms for TOMS [*Herman et al.*, 1997] and the Multiangle Imaging Spectroradiometer (MISR) [*Diner et al.*, 2001] are also capable of determining aerosol radiative effects over highly reflectant land surfaces such as desert.

[35] In this study, we use the TOMS Aerosol Index (AI) which provides a measure of the burden of partially absorbing atmospheric aerosols. The TOMS AI does not translate to τ_{aer} via a universal linear relationship, as it is dependent on the aerosol absorption properties and the altitude of the aerosol. *Hsu et al.* [1999] compared $\tau_{aer0.44}$ data from six AERONET sites in northwest Africa to TOMS AI and reported a linear relationship for each site. Here we use data from the two geographically most representative sites of Dakar and Cape Verde (close to the area marked SHADE in Figure 2c) and derive

$$\tau_{aer0.44} = 0.35(\text{TOMS AI}) + 0.095. \quad (3)$$

The $\tau_{aer\lambda}$ is deduced at all wavelengths by assuming that the size distribution shown in Figure 6 is representative of typical atmospheric dust size distributions, leading to the wavelength dependency of $k_{e\lambda}$ shown in Figure 7 which is linearly related to $\tau_{aer\lambda}$. $\tau_{aer\lambda}$ is normally reported at 0.55 μm and so we infer

$$\tau_{aer0.55} = 0.98\tau_{aer0.44} = 0.34(\text{TOMS AI}) + 0.093. \quad (4)$$

We also infer that

$$\tau_{aer10} = 0.33\tau_{aer0.55} \quad (5)$$

when the refractive indices of *Fouquart et al.* [1987] are used in the calculations and

$$\tau_{aer10} = 0.52\tau_{aer0.55} \quad (6)$$

when the refractive indices of *Volz* [1973] are used in the calculations which are useful in comparing τ_{aer} for solar and terrestrial wavelengths.

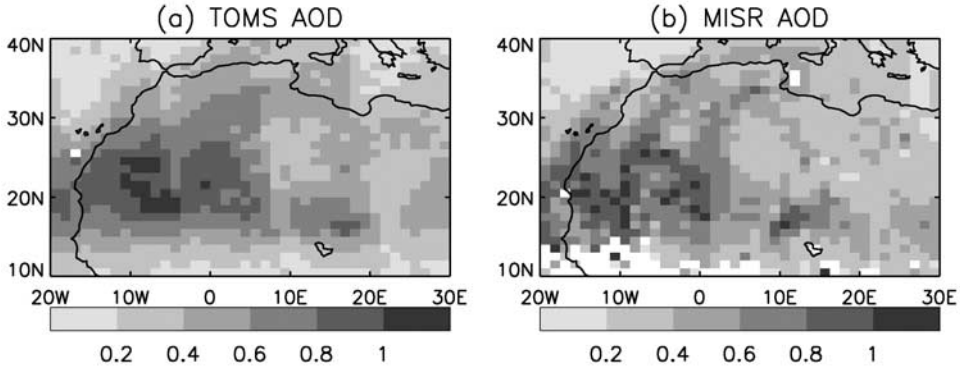

Figure 8. The $\tau_{aer0.55}$ derived for July 2003 for (a) TOMS and (b) MISR. In deriving the $\tau_{aer0.55}$ from TOMS, the TOMS AI is related to $\tau_{aer0.44}$ via equation (3), and the wavelength dependence of k_e shown in Figure 4a is used to derive $\tau_{aer0.55}$ via equation (4). The $\tau_{aer0.55}$ may be related to τ_{aer10} by equations (5) and (6). See color version of this figure in the HTML.

[36] Monthly mean TOMS AI are constructed from the daily TOMS AI data (available at http://toms.gsfc.nasa.gov/aerosols/aerosols.html) and rescaled to the NWP model grid. These data are converted from the semi-quantitative TOMS AI to $\tau_{aer0.55}$ by using the relationships detailed in equations (1) and (2). The TOMS $\tau_{aer0.55}$ for July 2003 is shown in Figure 8a. The $\tau_{aer0.55}$ shows a maximum over regions of the Sahara centered on approximately 20°N, 5°W where $\tau_{aer0.55}$ exceeds 1.4.

[37] TOMS AI data has the advantage that data are available over both land and ocean since 1978. However, as noted in the introduction some other dedicated aerosol instruments have been developed in recent years that determine $\tau_{aer0.55}$ over land. MISR is one such instrument and its multiangle viewing capability enables determination of $\tau_{aer0.55}$ even over bright desert surfaces [e.g., *Zhang and Christopher*, 2003]. The monthly mean MISR $\tau_{aer0.55}$ for July 2003 is shown in Figure 8b.

[38] Comparison of Figures 8a and 8b reveals the same general spatial distribution of $\tau_{aer0.55}$ but the TOMS data are much more diffuse than the MISR data. This is because the swath width from the TOMS instrument is relatively wide (3100 km) and consequently every area on the globe is sampled each day. MISR has a superior resolution, but a narrow swath width (360 km) which means that sampling over the region typically occurs once every five to six days. In addition, MISR does not retrieve $\tau_{aer0.55}$ in the presence of clouds. Nevertheless, we transform the TOMS $\tau_{aer0.55}$ and MISR $\tau_{aer0.55}$ onto the NWP model grid and perform a correlation between the two. The resulting scatterplot is shown in Figure 9 which shows a large amount of scatter. Much of this scatter is due to the poorer sampling statistics for MISR; the spatial inhomogeneity of Saharan dust plumes is extreme [e.g., *Tanré et al.*, 2003] so MISR may miss dust events at certain locations altogether. The following approximate linear relationship may be derived:

$$\text{TOMS } \tau_{aer0.55} = 1.03 \pm 0.28(\text{MISR } \tau_{aer0.55}) - 0.03 \pm 0.11 \cdot (r = 0.76). \quad (7)$$

Because the sampling statistics are better for TOMS $\tau_{aer0.55}$ and because the agreement between TOMS $\tau_{aer0.55}$ and MISR $\tau_{aer0.55}$ is close to 1:1, we use TOMS $\tau_{aer0.55}$ in the calculations that follow in section 8.

[39] Comparison of the TOMS $\tau_{aer0.55}$ shown in Figure 8a with the dOLRc shown in Figure 2c indicates that there is a reasonable correlation between the two. However, correlation alone does not establish cause and effect and the effects of aerosol on the OLR are investigated in a more rigorous manner in the sections that follow.

[40] The vertical profile of mineral dust is deduced from the measurements made by *Haywood et al.* [2003a]. These measurements were performed off the coast of West Africa during SHADE (see Figure 2c for the geographical position), and revealed the presence of a shallow, dust-free marine boundary layer below the mineral dust layer which had a clearly defined top at 500–600 hPa correlated to a strong hydrolapse. The hydrolapse shown in Figures 3a–3c occurs at a pressure of approximately 550 hPa, and therefore we apply a constant mass mixing ratio of mineral dust aerosol from the surface to 550 hPa. Such profiles have been shown to be representative over arid land surfaces where the strong surface heating causes strong vertical mixing [*Haywood et al.*, 2003c].

7. Direct Radiative Effects of Mineral Dust

[41] While it would be possible to estimate the effect of aerosols on the OLRc by applying them directly to the

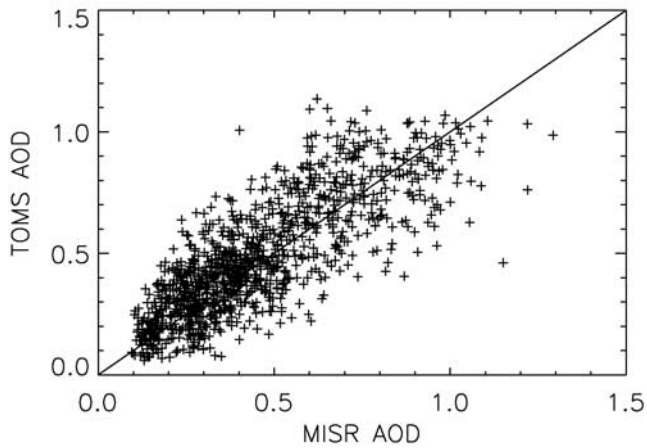

Figure 9. A scatterplot showing the correlation between $\tau_{aer0.55}$ from TOMS and $\tau_{aer0.55}$ from MISR.

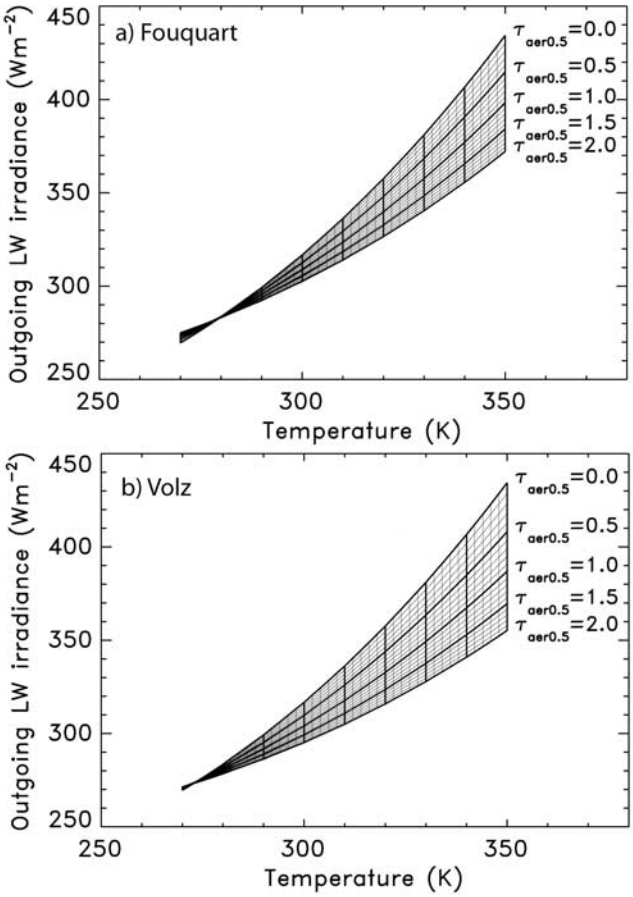

Figure 10. Graphical representation of the look-up-table for determining DRE_{LW} for refractive indices from (a) *Fouquart et al.* [1987] and (b) *Volz* [1973]. The *x* axis shows the surface temperature, and the *y* axis shows the top of the atmosphere clear sky OLRc. DRE_{LW} may be determined by $OLRc_{no\_aer} - OLRc_{aer}$.

NWP UM, here we choose to use an off-line version of the *Edwards and Slingo* [1996] radiative transfer code. The advantage of this approach is one of flexibility; the aerosol optical properties, concentrations and atmospheric profiles of temperature and humidity may be adjusted much more readily than in the full NWP model. The disadvantage of this approach is that the dynamical feedbacks due to aerosols affecting the radiation budget are difficult to assess. Nevertheless, the off-line radiative transfer modeling approach presented here is an important step in identifying whether the inclusion of aerosols within the NWP model are capable of explaining the dOLRc diagnosed in section 3.2.

[42] Because we are primarily interested in the cause of dOLRc, we first investigate the effect of aerosols directly upon OLRc by calculating the direct radiative effect in the longwave region of the electromagnetic spectrum, DRE_{LW}. We estimate the clear-sky DRE_{LW} as the difference between the top of the atmosphere OLRc with and without aerosols, i.e., $DRE_{LW} = OLRc_{no\_aer} - OLRc_{aer}$. $OLRc_{no\_aer}$ and $OLRc_{aer}$ are estimated using the *Edwards and Slingo* [1996] radiative transfer code. Aerosols also exert a significant perturbation to the solar radiation as evidenced by measurements of large values of DRE_{SW} at the top of the atmosphere [e.g., *Haywood et al.*, 2003a]. Aerosols reduce the solar radiation at the surface through a combination of scattering solar radiation back to space, and absorption of radiation leading to a significant direct radiative effect at the surface DRE_{SW_surf}. The reduction in the solar radiation at the surface will reduce the surface temperature, which will in turn further reduce the OLR. Thus, through land-surface feedback processes, the DRE_{SW} induces a DRE_{LW}. Here we define $DRE_{LWfeedback}$ as the additional perturbation to the OLR caused by the feedback effects of the DRE_{SW} on the surface temperature.

7.1. Calculations of DRE_{LW}

[43] The atmospheric profiles of temperature and humidity used as inputs to the radiative transfer code are the monthly mean radiosonde ascent from In Salah described in section 4, and the vertical profile of aerosol is described in section 7. Concentrations of all other atmospheric gases are set to current atmospheric values. The radiative transfer calculations are performed for surface temperatures ranging from 280–340 K, and for $\tau_{aer0.55}$ ranging from 0–2.0 to form a look-up-table shown graphically in Figures 10a and 10b using the refractive indices of *Fouquart et al.* [1987], and *Volz* [1973], respectively.

[44] Figures 10a and 10b show that in the absence of aerosol $OLRc_{no\_aer}$ ranges from approximately 270–434 Wm^{-2} for a surface temperature ranging from 280–340 K. These values encompass those shown in Figure 2b indicating that the radiative transfer calculations are representative of those in the NWP model. When $\tau_{aer0.55} = 2.0$, OLR_{aer} ranges from 275–372 Wm^{-2} in Figure 10a and 271–355 Wm^{-2} in Figure 10b for the same range in surface temperature. Thus the DRE_{LW} for $\tau_{aer0.55} = 2.0$ ranges from −5 Wm^{-2} at 270 K using the *Fouquart et al.* [1987] refractive indices to 80 Wm^{-2} at 340 K using the *Volz* [1973] refractive indices. A zero net radiative effect can be seen in each of Figures 10a and 10b when T_s is between 270–280 K; the inclusion of mineral dust has no effect on OLRc and hence DRE_{LW} is zero. This is because the effective emission temperature of the mineral dust is equivalent to T_s. If $\tau_{aer0.55} = 1.0$, which is reasonable for areas of the western Sahara desert (see Figure 8), then for surface temperatures of 320 K, 330 K, and 340 K the DRE_{LW} is 19 Wm^{-2}, 23 Wm^{-2}, and 29 Wm^{-2} using the *Fouquart et al.* [1987] refractive indices and 25 Wm^{-2}, 32 Wm^{-2}, and 39 Wm^{-2} using the *Volz* [1973] refractive indices.

[45] Figures 11a and 11b show the DRE_{LW} calculated from the look-up-table using the *Fouquart et al.* [1987] refractive indices and the *Volz* [1973] refractive indices respectively, using the monthly mean surface temperatures of Figure 4a and the $\tau_{aer0.55}$ from Figure 8a regridded onto the model grid. The data have been cloud-screened using the identical mask to that described in section 3.2 so that Figures 2 and 11 are directly comparable. Comparison reveals a similar general geographical pattern, although the magnitude of the maximum DRE_{LW} is some 20–40% less than the dOLRc. Thus, although inclusion of mineral dust in the terrestrial spectrum produces a DRE_{LW} that goes along way to explaining the dOLRc, it appears that DRE_{LW} alone does not completely account for the discrepancy. When using the refractive index of *Volz* [1973] there are

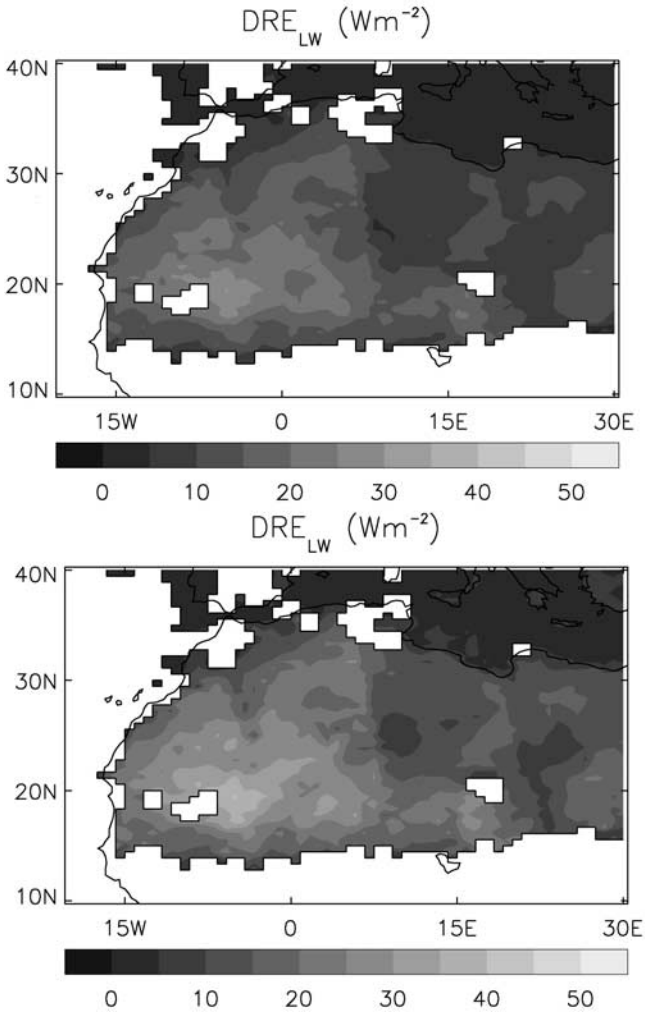

Figure 11. DRE_{LW} due to the radiative effect of mineral dust (Wm^{-2}) for refractive indices from (a) *Fouquart et al.* [1987] and (b) *Volz* [1973]. See color version of this figure in the HTML.

significantly greater areas where $DRE_{LW} > 20$ Wm^{-2} than where dOLRc > 20 Wm^{-2}.

7.2. Calculations of $DRE_{LWfeedback}$

[46] To estimate the effect that the presence of mineral dust has upon the solar radiation budget at the surface, the surface temperature and hence on OLRc, the *Edwards and Slingo* [1996] radiation code was run using 220-bands across the solar spectrum. Gaseous and aerosol atmospheric constituents were treated in a manner consistent with the radiative transfer calculations detailed in section 8.1. Radiative transfer calculations were performed with and without mineral dust aerosol for a range of $\tau_{aer0.55}$ and solar zenith angles. The Lambertian surface reflectance is set to a wavelength and solar zenith angle independent value of 0.30 which is typical of desert surfaces. The downwelling irradiance at the surface without aerosols, $SW_{surf\_no\_aer}$, and with aerosols, SW_{surf_aer}, are then calculated (Figure 12).

[47] The *Göttsche and Olesen* [2001] parameterization (section 5.1 and Figure 5) is fitted to the model data. Because the primary controller of the diurnal cycle in T_s is the irradiance at the surface (or the cosine of the solar zenith angle; see Figure 5) we then make the reasonable assumption that, in clear skies, the diurnal cycle of T_s is damped by the ratio of $SW_{surf\_aer}/SW_{surf\_no\_aer}$. For a solar zenith angle of 20°, $SW_{surf\_no\_aer}$ is approximately 1060 Wm^{-2}, while SW_{surf_aer} is 855 Wm^{-2} for a $\tau_{aer0.55}$ of 1. Thus, in this case, the damping in the diurnal range in temperature is a factor of approximately 0.81. The change in T_s at 1200 UTC calculated in this way indicates a cooling of up to approximately 10 K.

[48] Once the change in the T_s due to the radiative effects of dust in the solar spectrum has been calculated, the look-up-table shown in Figure 10 is used to calculate $DRE_{LWfeedback}$ which is shown in Figure 13. $DRE_{LWfeedback}$ is ~25–35% of DRE_{LW} and is therefore a second-order effect. In reality, our estimate of the temperature change via the change in the surface solar flux is likely to be the maximum possible effect because there will be an additional emission of longwave radiation to the surface caused by the presence of aerosol causing a surface warming. Therefore we suggest that our estimates of DRE_{LW} + $DRE_{LWfeedback}$ are likely to be an approximate maximum. Note that the additional effect of heating of the atmospheric column due to aerosol absorption in the solar region of the spectrum is implicitly accounted for in the NWP simulations as radiosonde ascents are assimilated which nudge the NWP profiles of temperature and humidity toward reality despite the lack of explicit representation of aerosol within the NWP model. We recognize that our method for diagnosing the response of T_s to the imposed aerosol perturbation is highly simplified; further work is required whereby aerosol is included explicitly within the NWP model which has an interactive surface scheme to diagnose the effects in a more consistent manner.

[49] Figure 14 shows the combined estimate of the effect of DRE_{LW} + $DRE_{LWfeedback}$. Figures 14a and 14b show the results when using the refractive indices of *Fouquart et al.* [1987] and *Volz* [1973], respectively. Comparison of DRE_{LW} + $DRE_{LWfeedback}$ (Figure 14) with dOLRc (Figure 2c) reveals the radiative effects of mineral dust can indeed explain much of the discrepancy in magnitude and spatial pattern between the observations of OLRc

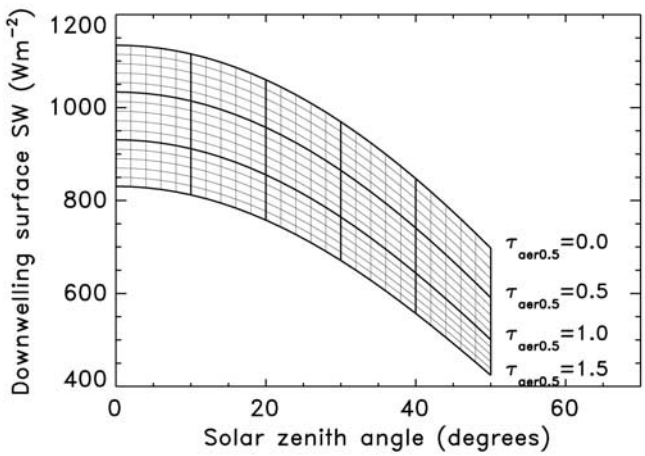

Figure 12. Graphical representation of the look-up-table for determining the ratio of SW_{surf_aer} to $SW_{surf\_no\_aer}$ and hence $DRE_{LW\_feedback}$ as described in the text.

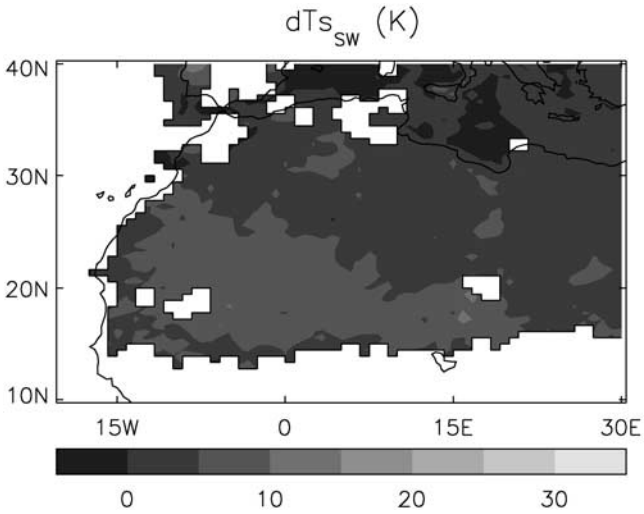

Figure 13. The change in model T_s (K) due to the reduction in SW_{surf}. See color version of this figure in the HTML.

from Meteosat-7 and those from the NWP model. Similarities and differences are discussed in the next section.

8. Discussion and Conclusions

[50] Geostationary satellite measurements show a significantly stronger atmospheric greenhouse effect over cloud-free desert regions of N.W. Africa than simulated by the Met Office NWP model. Monthly mean clear-sky OLRc from Meteosat-7 satellite data is up to 50 Wm^{-2} lower than model estimates during July 2003 when considering collocated 1200 UTC data. The available evidence suggests that although they could go some way to explaining the discrepancies in OLRc, potential surface temperature and emissivity errors in the model alone are unlikely to explain these differences. By building up a physically realistic model of the radiative properties of mineral dust and applying aerosol burdens that are derived from satellite instruments, we show that inclusion of the radiative effects of mineral dust is a plausible mechanism for reconciling the differences between Meteosat-7 measurements and the NWP model. Some differences clearly remain between our estimates of DRE and dOLRc. Generally our estimates of DRE_{LW} alone shown in Figure 11 do not fully capture the maximum dOLRc, while the spatial extent of significant DRE_{LW} (e.g., $DRE_{LW} > 10$ Wm^{-2}) is somewhat greater than that shown in dOLRc. When $DRE_{LW} + DRE_{LWfeedback}$ are considered together (Figure 14), the maximum dOLRc is relatively well represented both in geographic position, and in magnitude, (Figure 14b) the disagreement between $DRE_{LW} + DRE_{LWfeedback}$ and dOLRc becomes even worse over significant areas. However, we have clearly shown that the effect of mineral dust on the terrestrial radiation budget is significant, and potentially a larger effect than the effect of realistic representation of both surface temperature and surface emissivity.

[51] There are a few further caveats regarding the current study. For example, the lack of knowledge of the terrestrial refractive indices of mineral dust in the region is potentially a large source of error [*Sokolik et al.*, 1998]. That the relationship between τ_{aer10} and $\tau_{aer0.55}$ varies by a factor of 1.57 when the refractive indices of *Volz* [1973] replace those of *Fouquart et al.* [1987] (see equations (5) and (6)) shows that assumptions about the refractive indices of mineral dust in the longwave region of the spectrum are the single largest uncertainty in determining the aerosol radiative effects. Calculations show that for a T_s of 330 K and a $\tau_{aer0.55} = 1.0$, DRE_{LW} is 36.8 Wm^{-2} using the *Volz* [1973] refractive indices, but reduced to 24.6 Wm^{-2} using the *Fouquart et al.* [1987] refractive indices. Additionally, the exact details of the large modes of the aerosol size distribution from AERONET used in determining the radiative properties of mineral dust may not be entirely accurately characterized. This is because the AERONET radiometers measure the angular distribution of scattered radiances up to a wavelength of approximately 1 μm and radiances at 1 μm are not very sensitive to aerosols of 10 μm

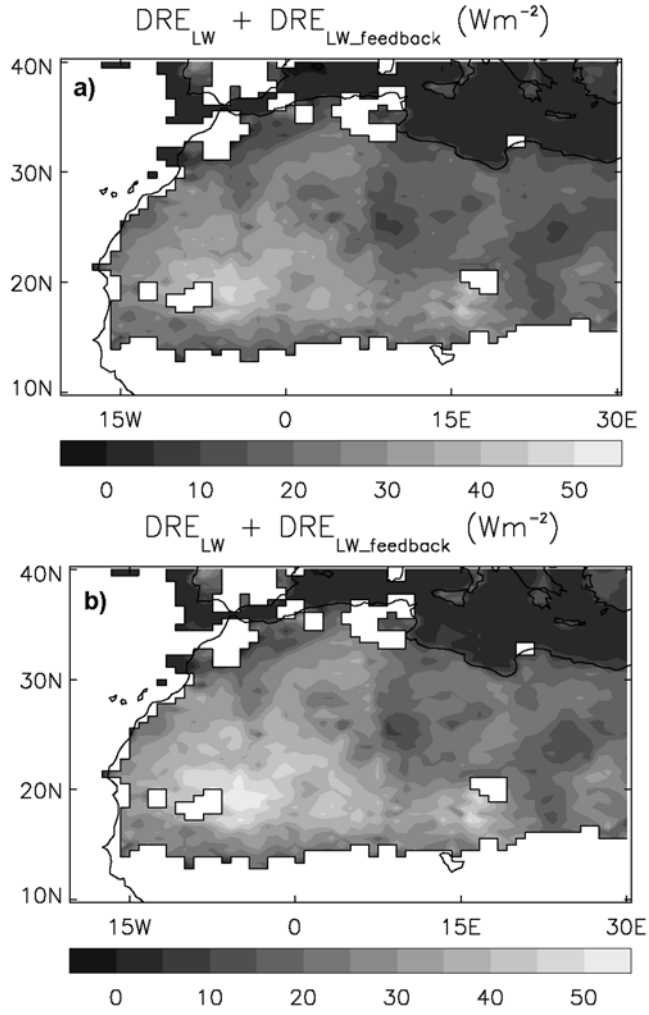

Figure 14. $DRE_{LW} + DRE_{LW\_feedback}$ (Wm^{-2}), which represents our best estimate of the radiative effect of mineral dust in the terrestrial spectrum, (a) using the refractive indices of *Fouquart et al.* [1987] and (b) using the refractive indices of *Volz* [1973]. The refractive indices of *WCP* [1986] are used in the solar spectral range as described in the text. See color version of this figure in the HTML.

radius. The assumption of spherical particles should not influence the radiative properties of the aerosol in the terrestrial region of the spectrum to a large extent. It is also acknowledged that the assumption of constant aerosol mass mixing ratio in the vertical is crude, but validation data are lacking. The estimation of dT_s due to the presence of mineral dust calculated here may not be entirely accurate because we consider only the effect of the aerosol on the solar radiation at the surface. There will be a further effect on T_s caused by the absorption and the reemission of terrestrial radiation by dust that will increase Ts, although this effect is probably most important in increasing the nighttime minimum Ts. Therefore our calculations of the change in T_s should be considered approximate maximum effects. It is possible that the Meteosat-7 cloud screening-algorithm may misclassify some large dust events with $\tau_{aer\lambda=0.55} > \sim 1.5$ as cloud. Indeed, the fact that the missing data in Figure 2 are close to the maximum $OLRc_{model}$-$OLRc_{Met7}$ are suggestive that this is indeed the case.

[52] There are only a few studies that have investigated the effect of mineral dust on LW irradiances over land regions. The most directly comparable studies to that presented here are those of *Zhang and Christopher* [2003], *Hsu et al.* [2000], and *Ackerman and Chung* [1992].

[53] *Zhang and Christopher* [2003] used MISR $\tau_{aer0.55}$ and LW irradiances from the Clouds and Earth Radiant Energy System (CERES) [*Wielicki et al.*, 1996] to investigate DRE_{LW} of Saharan dust over desert surfaces and derived a normalized DRE_{LW} over western Africa of 20 $Wm^{-2}/\tau_{aer0.55}$. *Zhang and Christopher* [2003] also performed sensitivity tests using the dust model from *Hess et al.* [1998] to determine the normalized DRE_{LW} for different aerosol scale heights, surface temperatures and atmospheric precipitable water. They perform calculations for an aerosol scale height of 2 km, a surface temperature of 316K, and a precipitable water content of 1.6 cm and determine a normalized DRE_{LW} of 18.7 $Wm^{-2}/\tau_{aer0.55}$. The precipitable water from the radiosonde at In Salah is approximately 1.2 cm, and analysis of Figure 10 reveals a corresponding normalized DRE_{LW} of between 15.6–22.2 $Wm^{-2}/\tau_{aer0.55}$ for the refractive indices of *Fouquart et al.* [1987], and *Volz* [1973], respectively indicating that our results are in good agreement. The diurnal cycle of surface temperature means that there is a diurnal cycle in DRE_{LW}. Using the T_s data shown in Figure 5, a diurnally averaged mean DRE_{LW} is 20.6 Wm^{-2} for a $\tau_{aer\lambda=0.55}$ of 1.0 is calculated while the corresponding maximum and minimum DRE_{LW} are 30.3 Wm^{-2} and 13.8 Wm^{-2} using the refractive indices of *Volz* [1973]. No changes in the atmospheric profile of temperature or humidity are accounted for in this estimate.

[54] *Hsu et al.* [2000] use a combination of ERBE and TOMS to derive a maximum instantaneous DRE_{LW} over land regions for July 1985 of -9.5 ± 1.5 Wm^{-2} per unit TOMS AI. Using a similar correlation between TOMS AI and TOMS τ_{aer} to that used in this study a DRE_{LW} of -36 $Wm^{-2}/\tau_{aer\lambda=0.44}$ is estimated which in reasonable agreement with the maximum DRE_{LW} of 30.3 $Wm^{-2}/\tau_{aer\lambda=0.55}$ derived in the previous paragraph.

[55] *Ackerman and Chung* [1992] used aerosol optical depths derived estimated from AVHRR by comparing the modeled brightness temperatures with those obtained from theoretical calculations and used estimates of the OLRc to derive an estimate of DRE_{LW} of between 20–50 Wm^{-2} over desert surfaces in the Arabian Peninsula, when $\tau_{aer0.55}$ ranges from 0.5–2.0. For a surface temperature of 316 K, they derive a normalized DRE_{LW} of between 12 and 23 $Wm^{-2}/\tau_{aer0.55}$ depending on the aerosol model used, results that are similar to our range of 15.6–22.2 $Wm^{-2}/\tau_{aer0.55}$ (see above).

[56] Thus, although our study uses independent measurements of aerosol size distribution, optical parameters and spatial distribution, the results in terms of normalized DRE_{LW} obtained are similar to those of *Ackerman and Chung* [1992], *Hsu et al.* [2000], and *Zhang and Christopher* [2003] and should therefore be considered robust.

[57] Analysis of preliminary data from the new GERB instrument [*Harries et al.*, 2005), which is onboard the Meteosat-8 satellite, is consistent with the Meteosat-7 observations presented in the present study [*Haywood et al.*, 2004]. The GERB instrument measures internally calibrated broadband radiances, which are currently undergoing validation; it is planned to exploit these data in conjunction with narrow band data from the Spinning Enhanced Visible and Infrared Imager (SEVIRI) instrument, also on board Meteosat-8, to measure more accurately the radiative effects of mineral dust aerosol.

[58] To conclude, this study shows that neglecting the radiative effects of mineral dust, may lead to the largest error in the NWP model estimates of the TOA OLR budget that is observed in the Meteosat-7 footprint. Further studies where mineral dust is incorporated directly into NWP models are planned and these should be able to assess the effect of mineral dust on the local and regional meteorology and climate.

[59] **Acknowledgments.** John Foot, Pete Francis, and Doug Parker are thanked for useful discussions on the effects of mineral dust on large-scale dynamics. Jean-Claude Thelen is thanked for maintaining the radiation code used in this study. The work was in part funded by the joint NERC/Met Office Connect-B grant NER/D/S/2002/00412.

References

Ackerman, S. A., and H. Chung (1992), Radiative effects of airborne dust on regional energy budgets at the top of the atmosphere, *J. Appl. Meteorol.*, *31*, 223–233.

Allan, R. P., and M. A. Ringer (2003), Inconsistencies between satellite estimates of longwave cloud forcing and dynamical fields from reanalyses, *Geophys. Res. Lett.*, *30*(9), 1491, doi:10.1029/2003GL017019.

Bertrand, C., N. Clerbaux, A. Ipe, and L. Gonzalez (2003), Estimation of the 2002 Mount Etna eruption cloud radiative forcing from Meteosat-7 data, *Remote Sens. Environ.*, *87*, 257–272.

Boucher, O., et al. (1998), Intercomparison of models representing direct shortwave radiative forcing by sulfate aerosols, *J. Geophys. Res.*, *103*, 16,979–16,998.

Clerbaux, N., S. Dewitte, L. Gonzalez, C. Bertrand, B. Nicula, and A. Ipe (2003), Outgoing longwave flux estimation: Improvement of angular modelling using spectral information, *Remote Sens. Environ.*, *85*, 389–395.

Diner, D. J., W. A. Abdou, J. E. Conel, K. A. Crean, B. J. Gaitley, M. Helmlinger, R. A. Kahn, J. V. Martonchik, and S. H. Pilorz (2001), MISR aerosol retrievals over southern Africa during the SAFARI-2000 dry season campaign, *Geophys. Res. Lett.*, *28*, 3127–3130.

Dubovik, O., and M. D. King (2000), A flexible inversion algorithm for retrieval of optical properties from Sun and sky radiance measurements, *J. Geophys. Res.*, *105*, 20,673–20,696.

Dubovik, O., B. N. Holben, T. Lapyonok, A. Sinyuk, M. I. Mishchenko, P. Yang, and I. Slutsker (2002), Non-spherical aerosol retrieval method employing light scattering by spheroids, *Geophys. Res. Lett.*, *29*(10), 1415, doi:10.1029/2001GL014506.

Dunion, J. P., and C. S. Velden (2004), The impact of the Saharan Air Layer on Atlantic tropical cyclone activity, *Bull. Am. Meteorol. Soc.*, *85*, 353–365, doi:10.1175/BAMS-85-3-353.

Edwards, J. M., and A. Slingo (1996), Studies with a flexible new radiation code: I. Choosing a configuration for a large scale model, *Q. J. R. Meteorol. Soc.*, *122*, 689–720.

Fouquart, Y., B. Bonnel, G. Brogniez, J. C. Buriez, L. Smith, and J. J. Morcrette (1987), Observations of Saharan aerosols: Results of ECLATS field experiment: Part II: Broadband radiative characteristics of aerosols and vertical flux divergence, *J. Clim. Appl. Meteorol.*, *26*, 38–52.

Göttsche, F.-M., and F.-S. Olesen (2001), Modelling of diurnal cycles of brightness temperature extracted from METEOSAT data, *Remote Sens. Environ.*, *76*, 338–349.

Harries, J. E., et al. (2005), The Geostationary Earth Radiation Budget (GERB) Experiment, *Bull. Am. Meteorol. Soc.*, in press.

Haywood, J. M., P. N. Francis, M. D. Glew, and J. P. Taylor (2001), Optical properties and direct radiative effect of Saharan Dust: A case study of two Saharan dust outbreaks using aircraft data, *J. Geophys. Res.*, *106*, 18,417–18,428.

Haywood, J., P. Francis, S. Osborne, M. Glew, N. Loeb, E. Highwood, D. Tanré, G. Myhre, P. Formenti, and E. Hirst (2003a), Radiative properties and direct radiative effect of Saharan dust measured by the C-130 aircraft during SHADE: 1. Solar spectrum, *J. Geophys. Res.*, *108*(D18), 8577, doi:10.1029/2002JD002687.

Haywood, J., P. Francis, O. Dubovik, M. Glew, and B. Holben (2003b), Comparison of aerosol size distributions, radiative properties, and optical depths determined by aircraft observations and Sun photometers during SAFARI 2000, *J. Geophys. Res.*, *108*(D13), 8471, doi:10.1029/2002JD002250.

Haywood, J. M., S. R. Osborne, P. N. Francis, A. Keil, P. Formenti, M. O. Andreae, and P. H. Kaye (2003c), The mean physical and optical properties of regional haze dominated by biomass burning aerosol measured from the C-130 aircraft during SAFARI 2000, *J. Geophys. Res.*, *108*(D13), 8473, doi:10.1029/2002JD002226.

Haywood, J. M., R. P. Allan, I. Culverwell, A. Slingo, S. Milton, and J. E. Edwards (2004), Can desert dust explain the anomalous greenhouse effect observed over the Sahara during July 2003 revealed by GERB/UM intercomparisons?, *MRF Tech. Note 49*, Obs. Res. Met Off., Exeter, Devon, UK.

Herman, J. R., P. K. Bhartia, O. Torres, C. Hsu, C. Seftor, and E. Celarier (1997), Global distribution of UV-absorbing aerosols from Nimbus 7/TOMS data, *J. Geophys. Res.*, *102*, 16,911–16,922.

Hess, M., P. Koepke, and I. Schult (1998), Optical properties of aerosols and clouds: The software package OPAC, *Bull. Am. Meteorol. Soc.*, *79*, 831–844.

Highwood, E. J., J. M. Haywood, M. D. Silverstone, S. M. Newman, and J. P. Taylor (2003), Radiative properties and direct effect of Saharan dust measured by the C-130 aircraft during Saharan Dust Experiment (SHADE): 2. Terrestrial spectrum, *J. Geophys. Res.*, *108*(D18), 8578, doi:10.1029/2002JD002552.

Holben, B. N., et al. (1998), AERONET: A federated instrument network and data archive for aerosol characterization, *Remote Sens. Environ.*, *66*, 1–16.

Hsu, N. C., J. R. Herman, O. Torres, B. N. Holben, D. Tanré, T. F. Eck, A. Smirnov, B. Chatenet, and F. Lavenu (1999), Comparison of the TOMS aerosol index with Sun-photometer aerosol optical thickness: Results and applications, *J. Geophys. Res.*, *104*, 6269–6279.

Hsu, N. C., J. R. Herman, and C. Weaver (2000), Determination of radiative forcing of Saharan dust using combined TOMS and ERBE data, *J. Geophys. Res.*, *105*, 20,649–20,662.

Ipe, N. Clerbaux, C. Bertrand, S. Dewitte, and L. Gonzalez (2004), Validation and homogenisation of cloud optical depth and cloud fraction retrievals for GERB/SEVIRI scene identification using Meteosat-7 data, *Atmos. Res.*, *72*, 17–37, doi:10.1016/j.atmosres.2004.03.010.

Lorenc, A. C., et al. (2000), The Meteorological Office global three-dimensional variational data assimilation scheme, *Q. J. R. Meteorol. Soc.*, *126*(570), 2991–3012.

Mishchenko, M. I., I. V. Geogdzhayev, L. Liu, J. A. Ogren, A. A. Lacis, W. B. Rossow, J. W. Hovenier, H. Volten, and O. Muñoz (2003), Aerosol retrievals from AVHRR radiances: Effects of particle nonsphericity and absorption and an updated long-term global climatology of aerosol properties, *J. Quant. Spectrosc. Radiat. Transfer*, *79/80*, 953–972.

Myhre, G., et al. (2004), Intercomparison of satellite retrieved aerosol optical depth over the ocean, *J. Atmos. Sci.*, *61*, 499–513.

Prigent, C., F. Aires, and W. B. Rossow (2003), Land surface skin temperatures from a combined analysis of microwave and infrared satellite observations for an all-weather evaluation of the differences between air and skin temperatures, *J. Geophys. Res.*, *108*(D10), 4310, doi:10.1029/2002JD002301.

Snyder, W. C., Z. Wan, Y. Zhang, and Y.-Z. Feng (1998), Classification-based emissivity for land surface temperature measurement from space, *Int. J. Remote Sens.*, *19*, 2753–2774.

Sokolik, I. N., O. B. Toon, and R. W. Bergstrom (1998), Modelling the radiative characteristics of airborne mineral aerosols at infrared wavelengths, *J. Geophys. Res.*, *103*, 8813–8826.

Sutherland, R. A. (1986), Broadband and spectral emissivities (2–18 um) of some natural soils and vegetation, *J. Atmos. Ocean. Technol.*, *3*(1), 199–202.

Tanré, D., J. Haywood, J. Pelon, J. F. Léon, B. Chatenet, P. Formenti, P. Francis, P. Goloub, E. J. Highwood, and G. Myhre (2003), Measurement and modeling of the Saharan dust radiative impact: Overview of the Saharan Dust Experiment (SHADE), *J. Geophys. Res.*, *108*(D18), 8574, doi:10.1029/2002JD003273.

Thorncroft, C. D., et al. (2003), The JET2000 project: Aircraft observations of the African easterly jet and African easterly waves, *Bull. Am. Meteorol. Soc.*, *84*, 337–351.

Volz, F. E. (1973), Infrared optical constants of ammonium sulphate, Sahara dust, volcanic pumice and flyash, *Appl. Opt.*, *12*(3), 564–567.

Wielicki, B. A., B. R. Barkstrom, E. F. Harrison, R. B. Lee III, G. L. Smith, and J. E. Cooper (1996), Clouds and the Earth's Radiant Energy System (CERES): An Earth observing system experiment, *Bull. Am. Meteorol. Soc.*, *77*, 853–868.

World Climate Program (WCP) (1986), A preliminary cloudless standard atmosphere for radiation computation, World Meteorol. Org., Geneva.

Zhang, J., and S. A. Christopher (2003), Longwave radiative forcing of Saharan dust aerosols from MODIS, MISR, and CERES observations on Terra, *Geophys. Res. Lett.*, *30*(23), 2188, doi:10.1029/2003GL018479.

R. P. Allan and T. Slingo, Environmental Systems Science Centre, University of Reading, Reading, UK.

N. Clerbaux, Royal Meteorological Institute of Belgium, Brussels, Belgium.

I. Culverwell, J. Edwards, J. M. Haywood, and S. Milton, Met Office, W080, Cordouan 2, FitzRoy Road, Exeter EX1 3PB, UK. (jim.haywood@metoffice.gov.uk)